Geoscience Frontiers 15 (2024) 101723

Contents lists available at ScienceDirect

Geoscience Frontiers

journal homepage: www.elsevier.com/locate/gsf

Research Paper

The formation and growth mechanisms of young back-arc spreading ridges from high-resolution bathymetry: The Marsili Seamount (Tyrrhenian Sea, Italy)

Eugenio Nicotra [a,*], Salvatore Passaro [b], Guido Ventura [c,d]

[a] Dipartimento di Biologia Ecologia e Scienze della Terra, Università della Calabria, 87036 Arcavacata di Rende, Cosenza, Italy
[b] Istituto di Scienze Marine CNR, 80133 Napoli, Italy
[c] Istituto Nazionale di Geofisica e Vulcanologia, 00143 Roma, Italy
[d] Istituto per lo Studio degli impatti Antropici e Sostenibilitá in ambiente marino CNR, 91026 Capo Granitola, Trapani, Italy

ARTICLE INFO

Article history:
Received 26 May 2023
Revised 30 August 2023
Accepted 4 October 2023
Available online 7 October 2023
Handling Editor: Inna Safonova

Keywords:
Back-arc spreading ridge
Morphology
Tectonics
Volcanism
Marsili seamount

ABSTRACT

The formation and growth mechanisms of Mid-Ocean Ridges (MOR) are relatively well known, whereas those of back-arc spreading ridges are comparatively less known because geophysical, geochemical, and morphological data are scarce and of low density. Here we present a high-resolution bathymetry of the Marsili Seamount (MS; 1 Ma – 3 ka), which represents the inflated spreading ridge of the 2 Ma old Marsili back-arc basin associated to the subduction of the Ionian Sea below the Calabrian Arc and Tyrrhenian Sea. MS is 70 km long, 30 km wide, and its height reaches about 3000 m from surrounding seafloor. Our new digital bathymetric model has a 5 m grid cell size resolution and covers the MS bathymetry from −1670 mbsl to the top at −491 mbsl. We conduct morphometric and morphological analyses of the bathymetry and recognize landforms due to volcanic, tectonic, hydrothermal and gravity processes. MS consists of volcanoes related to fissural and central-type activity, this latter located at the northern and southern tips of the main dike swarms. Dike swarms represent the surface expression of different ridge segments whose strikes are controlled by the larger scale back-arc spreading processes and by the local occurrence of an active hydrothermal field. This latter develops in a flat area between two partly overlapping ridge segments where historical volcanism and extensional processes concentrate. Such ridges represent the embryonic stage of the formation of transform-like faults. Central volcanoes, the northern of which is characterized by a caldera, form at the tips of MS because the decrease in width of the major volcanic fissures promotes vent localization associated with the formation of sill-like reservoirs from which central-type vents may develop. Gravity processes affecting the MS flanks are due to shallow seafloor sliding. Caldera collapses affecting the northernmost central-type polygenic volcano must be included in the evaluation of the hazard related to potential tsunami. Inward dipping faults characterize the MS eastern flank suggesting a moderately asymmetric growth of the spreading ridge possibly associated with the eastward opening of the Marsili back-arc.

The Marsili back-arc spreading rate is similar to those of MOR slow spreading ridges. However, the MS morphology resembles that of fast spreading ridges. These two features also characterize more extended back-arc spreading ridges (e.g. the Mariana in Western Pacific). We conclude that, independently from the spatial scale, the increase in the ridge accretion rate is related to the progressive addition of a subduction-related component to a pure spreading mantle source.

1. Introduction

Back-arc basins (BAB) are a component of the subduction factory focusing extensional processes at convergent plate margins (Karig, 1971; Stern, 2002; Artemieva, 2023). BAB develop in the overriding plate and are characterized by crustal stretching, seafloor spreading and volcanism. The composition of the BAB basalts frequently reflect the involvement of both mantle and slab components being BAB located near volcanic arcs. The formation and evolution of BAB is primarily controlled by the relative motion of the trench and overriding plate (e.g., slab roll-back) which, in turn,

* Corresponding author.
E-mail address: eugenio.nicotra@unical.it (E. Nicotra).

https://doi.org/10.1016/j.gsf.2023.101723

moves in response to different thermal, mechanical, and kinematic mechanisms (Sdrolias and Muller, 2006; Li et al., 2018; Holt and Royden, 2020; Wei and Wiens, 2020). According to Schliffke et al. (2022) and Artemieva (2023), the formation of BAB spreading ridges easily occurs in oceanic plates while it requires larger stretching rates and longer times in continental plates. With respect to the Mid-Ocean ridges (MOR) at divergent plate boundaries, for which a large amount of geophysical, geochemical, and morphological data is available (Solomon and Toomey, 1992; Kelley et al., 2002; Tan et al., 2016; Maher et al., 2021), the morphology of BAB spreading ridges is, with few exceptions (Anderson et al., 2017; Caratori Tontini et al., 2019), comparatively less known. In particular, open questions concern the occurrence (or not) and the causes of BAB ridge segmentation, the origin of possible transform faults, the along-axis faulting style, the morphologies of the volcanic landforms (i.e., central vs monogenetic/-fissural vents), and, more in general, the relationships among the spreading rate and accretion rate due to magma output. Furthermore, another important open question regards the episodicity of BAB, related to their existence for a limited amount of time and then deformation abruptly jumps into a new location with the formation of a new basin (e.g., the Vavilov-Marsili transition in Southern Tyrrhenian Sea; cf. Schliffke et al., 2022). Here we present a morphometric and morphological analysis of a high resolution (5 m × 5 m) Digital Bathymetric Model (DBM) of the still active Marsili seamount (MS, Southern Tyrrhenian Sea, Italy), which represents the inflated spreading ridge of the 2 Ma old Marsili BAB associated to the Ionian Sea subduction below the Calabrian Arc and Tyrrhenian Sea (Fig. 1; Savelli, 2001; Marani et al., 2004; Cocchi et al., 2009; Ventura et al., 2013; Cocchi et al., 2017). Our aim is the analysis of the MS landforms, and specifically to (a) recognize the morphological and geological features and (b) understand how volcanoes, overlapping vs. segmented spreading centers and faults interact and control the growth and evolution of BAB spreading ridges.

2. Geodynamic and geological setting

The Southern Tyrrhenian Sea (STS) is located in the central-western Mediterranean area, affected by crustal extension in its northern sector and seafloor spreading in the southern one (Rosenbaum and Lister, 2004). The STS opening is associated with the south-eastward migration of the Calabrian-Sicily arc system in response to the subduction of the Ionian oceanic lithosphere (Fig. 1; Sartori, 2003) and, in particular, to the process of roll-back of the 70°–80° northwest dipping and up to 500 km deep Ionian slab (Doglioni, 1991; Doglioni et al., 1997; Panza et al., 2007; Carminati et al., 2012). This latter is delimited by two STEP (Subduction-Transform-Edge-Propagator) faults to the north and east (Cocchi et al., 2017). The STS seafloor spreading led to the formation of two main ocean-like BABs: the Vavilov BAB (4.3 – 2.6 Ma; Kastens and Mascle, 1990), which is located in the northern Thyrrenian sector (Fig. 1), and the Marsili BAB (1.8 – 0.2 Ma; Savelli, 2001) in the southern one (Fig. 1). The Aeolian Islands and the associated seamounts, which represent the volcanic arc associated to the Ionian Sea-Calabrian Arc subduction, bound the southern and eastern sectors of the Marsili BAB (Fig. 1)

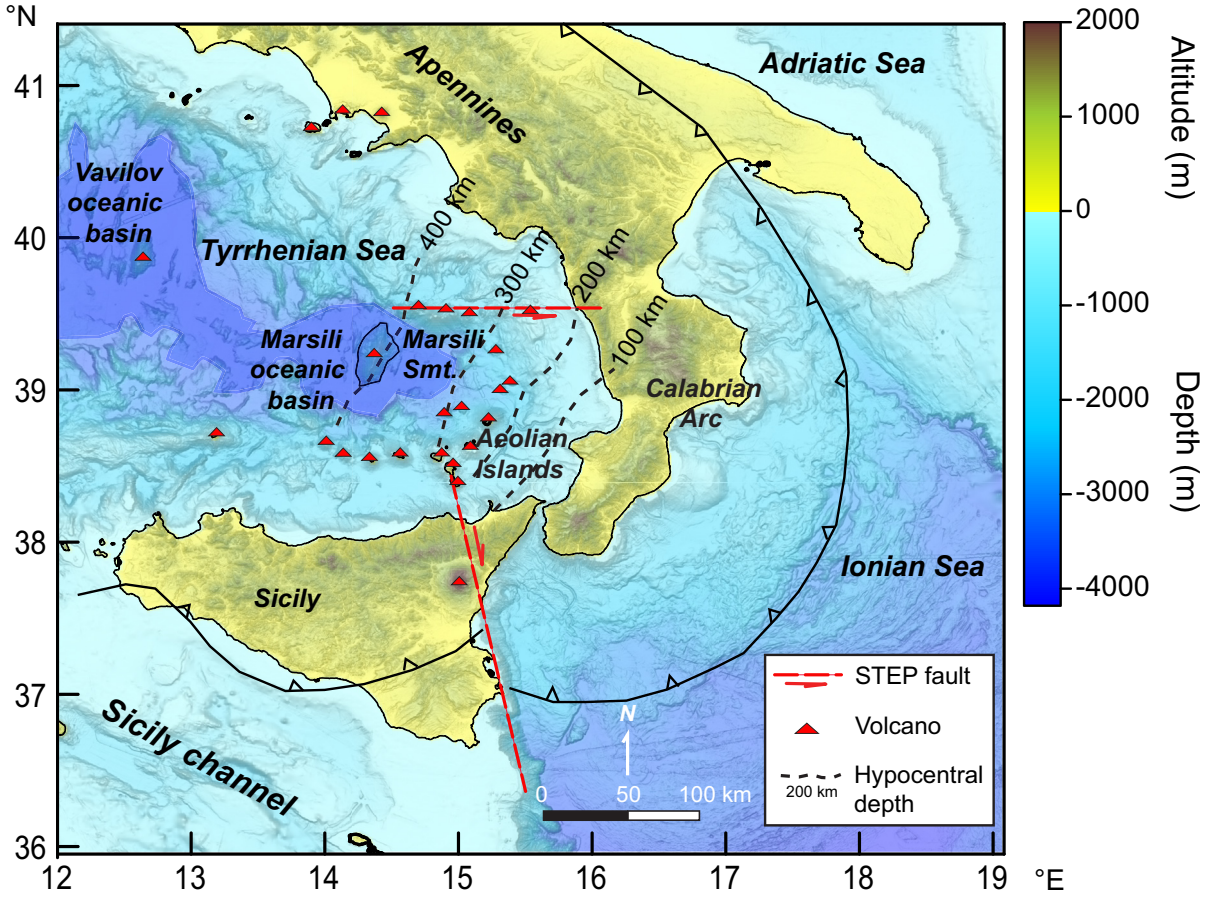

Fig. 1. Geodynamic framework of the Southern Tyrrhenian Sea and Calabrian Arc (Southern Italy). The depth of the earthquakes (in km) along the Ionian slab is reported as a dashed line. Data from De Astis et al. (2003) and Cocchi et al. (2017). The background digital terrain model is from EMODnet (https://emodnet.ec.europa.eu/en/bathymetry).

(Beccaluva et al., 1982; Faccenna et al., 1997; Nicotra et al., 2014). Volcanism and hydrothermal vents characterize the Marsili BAB at variable depths (Aliani et al., 2010; Lupton et al., 2011; Esposito et al., 2018). Volcanic features include axial and central volcanoes characterized by explosive and effusive activity (Passaro et al., 2010; Cocchi et al., 2017; Iezzi et al., 2020) associated with magmas of different composition (Lustrino et al., 2011; Iezzi et al., 2013, 2020; Tamburrino et al., 2015). The Marsili Seamount (MS) is a 70 km × 20 km extended, NNW–SSE elongated volcanic complex rising 3000 m from the seafloor up to about −500 mbsl (Fig. 2). MS represents the spreading ridge of the Marsili BAB (Marani and Trua, 2002) and formed in the last 1 Ma on a 10 to 12 km thick oceanic crust (Magrini et al., 2022). Marani and Trua (2002) proposed that MS represents an inflated spreading center. The more recent MS activity is dated at about 2–3 ka BP and the vent responsible for this last explosive eruption has been identified in the central-northern sector of the volcano (Iezzi et al., 2013, 2020; Tamburrino et al., 2015). The present activity is characterized by shallow seismicity and hydrothermal emissions (D'Alessandro et al., 2009; Lupton et al., 2011). According to Cocchi et al. (2009), the MS accretion rate was between 2.1 × 10^{-3} km^3/yr and 3.4 × 10^{-3} km^3/yr during the late Matuyama and Jaramillo Chrons, while during the Brunhes Chron the rate increased to 4.21 × 10^{-3} km^3/yr^{-1}. The increasing of MS accretion rate with decreasing time was coeval to a decrease of the Marsili BAB opening rate (from 3 cm/yr to about 1.8 cm/yr). In a previous study of a 25 m × 25 m DBM of MS, Ventura et al. (2013) identified signs of seafloor failures and coexisting central-type and fissure volcanoes with prevailing passive magma ascent mechanisms mainly controlled by tectonic forces. They propose that (a) the late MS volcanism concentrates along pre-existing fractures inherited by early spreading activity and (b) MS is a volcanic arc volcano emplaced on an older, 'relict' BAB spreading ridge.

3. Methods

3.1. Bathymetry

High Resolution (HR) multibeam swath bathymetry data have been acquired during the Aeolian_2010 oceanographic cruise (R/V Urania, National Research Council) with a Simrad EM 710 multibeam equipment (Konigsberg) with a 70–100 KHz acoustic source frequency, 400 soundings per swath, and 140° of pulse width. The data acquisition has been carried out with Differential Global Positioning System and by determining speed of sound in seawater with sound velocity probes recorded every 6–8 h and applied in real-time during the surveys. Raw data have been processed by applying corrections for sound velocity and tidal effects. Spike and erroneous subsets of soundings have been filtered by using the Caris Hips and Sips standard software suite (https://www.teledynecaris.com/en/products/hips-and-sips/). The final Digital Bathymetric Model (DBM) of MS has been constructed by ordinary gridding following Cressie (1990). DBM has a 5 m grid cell size resolution and reports measurements included between −491 m and −1670 m below the sea level (b.s.l.)(Fig. 2).

3.2. Morphometric parameters

The morphometric analysis of the DBM has been carried out by calculating the following parameters: slope, aspect, convergence index (CI, Claps et al., 1996), and geomorphons (GEOM; Jasiewicz

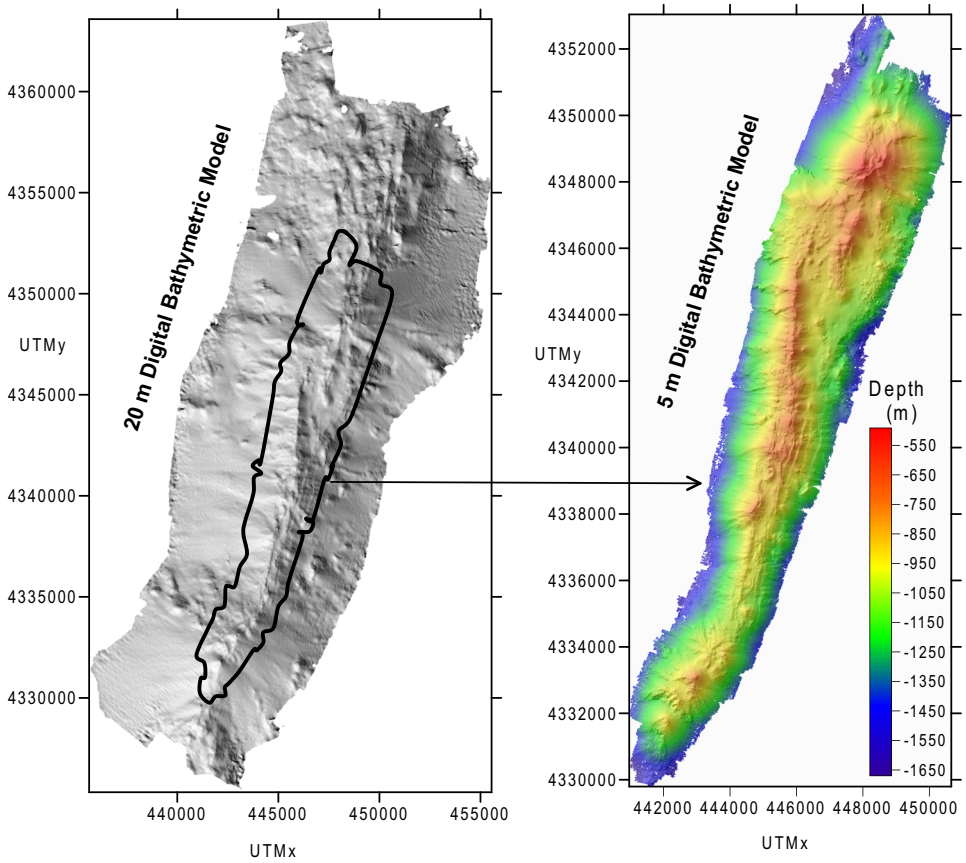

Fig. 2. Left: Shaded relief of the 25 m resolution DBM of the Marsili Seamount from Ventura et al. (2013). Right: Shaded relief of the 5 m resolution DBM elaborated from data acquired in this study (see Section 3.1 for details on the data acquisition and elaboration).

and Stepinski, 2013). These parameters have been determined with the SagaGIS software (Conrad et al., 2015; https://saga-gis.sourceforge.io). CI identifies the convergent (channels) and divergent (ridges) areas. It represents the difference in aspect values between the central cell and those surrounding 8 cells using a set of moving windows. It has positive values for ridges, negative values for channels, and CI = 0 for flat areas. GEOM (geomorphologic phenotypes) are recognized on the basis of a pattern recognition analysis and include the following classes: flat, peak or summit, ridge, shoulder, spur, slope, hollow, footslope, valley and pit or depression. To obtain a view of the larger scale morphology of the MS, we apply a low-pass filter with a cut-off at 300 m to the original 5 m × 5 m DBM, in order to remove the high-frequency topographic features. These maps have been used to derive a geomorphological model of MS in which the main volcanic, structural, and gravity landforms are reported. The results of the above described morphometric analysis are reported in Figs. 2–7, whereas morphological elements of MS are shown in Figs. 8 and 9.

4. Results

The results of the morphometric analysis are reported in Figs. 2–7. In the following, depths are expressed in m below the sea level (mbsl). Our volcanic, geological and geomorphological data confirm the hypothesis of subdivision of MS in 4 sectors proposed by Ventura et al. (2013). However, the DBM of Ventura et al. (2013) was more extended in depth and with a significantly lower resolution (25 m × 25 m), so this subdivision has been here refined in Fig. 5a (Sectors A, B, C, D). In the following sections we will describe the peculiar volcanic, geological and geomorphological elements of each sector.

4.1. Morphometric data

The DBM covers a depth interval between −491 m and −1670 mbsl with the more representative values at −1000 m (Fig. 3a). Although the slope ranges between 3° and 78°, most of MS presents a most frequent slope of 28° (Figs. 3b and 4). The distribution of the aspect values reveals that MS is characterized by a nearly symmetric structure defined by two elongated, sub-parallel flanks striking NNW–SSE with the western and eastern flanks dipping toward N100° and N290°, respectively (Figs. 3c and 4). Fig. 3d highlights that the MS flanks, which develop between −1400 m and −800 mbsl, do not show significant variations of the aspect values with depths.

The slope values slightly increase with increasing depths. Between −800 m and −400 mbsl, the slope is nearly constant with most values within the range of 20°–32°. Between −800 m and −1100 mbsl, a relatively low slope area with values < 16° has been identified. This area includes the top of the MS Sector C (Figs. 2 and 4). Fig. 3f reveals that the more representative slope values for the MS flanks range between 18° and 32°. The aspect map in Fig. 4 clearly evidences some up to 3 km long, ENE dipping rectilinear scarps outcropping in the eastern, ESE dipping flank of the MS Sector B (Figs. 2 and 4). Elongated strips of low slope (0°–15°) also occur at the top of MS, mainly in the Sectors B and C.

The maps of CI and GEOM (Fig. 4) clearly show the prevalent, up to −500 m wide ridge-like structure of MS. In particular, these maps depict a well-developed, about 14 km long ridge extending from the southern Sector B of MS to the central-northern Sector C (Figs. 2 and 4; sectors subdivision at Fig. 5a). Here, the ridge interrupts and another, sub-parallel, 2 km long and −50 to −100 m wide ridge occurs. The two ridges are separated by a relatively flat area, having a surface of about 10 km^2 (Fig. 4). The strike of the MS main ridge (Sector B; Figs. 2, 4 and 5a) is not constant and changes from N40°E in the southern sector to N20°E in the central-northern sector. Northward, at its northern tip, it is N20°E. The other, 2 km long ridge shows a N–S strike in its southern sector and a N20°E strike in the northern one. All the above described changes in the strike of the two ridges are sharp and without morphological evidence of bend-like connections. The maps of Fig. 4 do not show well-developed, incised valleys, while elongated concave-upward hollows with strikes mainly orthogonal to the MS ridge main elongation may be recognized. In addition, partly dismantled and large (diameter of about 1 km) cone-like structures may be detected in the southern sector of MS (Fig. 2), while a larger cone (diameter of about 2 km) with an articulated morphology characterizes the MS northern sector. Smaller, often aligned cones are also present (Fig. 2). The low-pass filter map of Fig. 5 depicts the larger scale morphological structure of MS. This map well evidences the two above described MS ridges and depicts a less developed, third ridge-like structure located in the sector D of MS, where the largest MS volcanic edifice is located. This suggests that this volcano also develops, at least in part, on a N20°E elongated ridge.

4.2. MS landforms

The large-scale morphology of the MS ridge clearly defines it as a volcanic complex, i.e. an ensemble of spatially associated volcanic and volcano-tectonic structures. The 5 m × 5 m DBM allows us to identify several details of the MS morphology and we distinguish landforms related to different processes. These landforms are detailed here below.

4.2.1. Volcanic and volcano-tectonic landforms

The analysis of the 2D and 3D views of the MS DBM reveals the following volcanic landforms: eruptive vents (eruptive fissures, dykes, volcanic cones, central volcanoes), volcanic products (lava flows and lava flow fields), volcano-tectonic structures (calderas, also nested), faults, collapse scar (and relative deposits) and hydrothermal mounds. All these elements are shown in Figs. 8 and 9. Their density of occurrence, orientation and shape substantially change within the four previously indicated sectors of MS.

The dominant type of eruptive vents of the recent activity of MS develops along fissures. These are defined by tens of small volcanic cones aligned within narrow dyke-induced grabens.

In general, by grouping cones belonging to the same fissure we identify 11 segments with 0.5 km to 3 km overall extensions (Fig. 9). Following the morphological criteria of Smith and Németh (2017), the morphological analysis suggests that eruptive fissures at MS can be considered as monogenetic, also because of their small size and lack of morphological evidence of polyphasic growth (e.g., scars, changes in slope). The main strike of the eruptive fissures varies from NNE–SSW in sector B to NE–SW (N°30E) in sector C, with the two strikes contemporaneously present in the latter sector (Fig. 7b and 9). Eruptive fissures consist of tens (>15) of aligned small volcanic edifices with a conical shape and a crater on the top, a feature very similar to the typical subaerial scoria cones (Fig. 8). Considering that an eruptive fissure is the surface expression of a an intruded dyke, the presence of these small volcanic structures suggests a scenario in which the eruptions started with a linear vent (equivalent to the subaerial "fire curtains") that progressively evolves to smaller, punctual vents in a way similar to the typical Icelandic-like eruptions. Typical of eruptive fissures are also the dyke-induced grabens (Drymoni et al., 2013). These latter, well defined in the DBM, are characterized by width values smaller than 200 m (Figs. 8–9). Eruptive fissures represent the dominant volcanic landform in sectors B and C, whereas they are lacking in the other two MS sectors (Fig. 9).

Eruptive fissures of sector B present a dominant, highly rectilinear N–S strike. In particular, five different eruptive episodes have con-

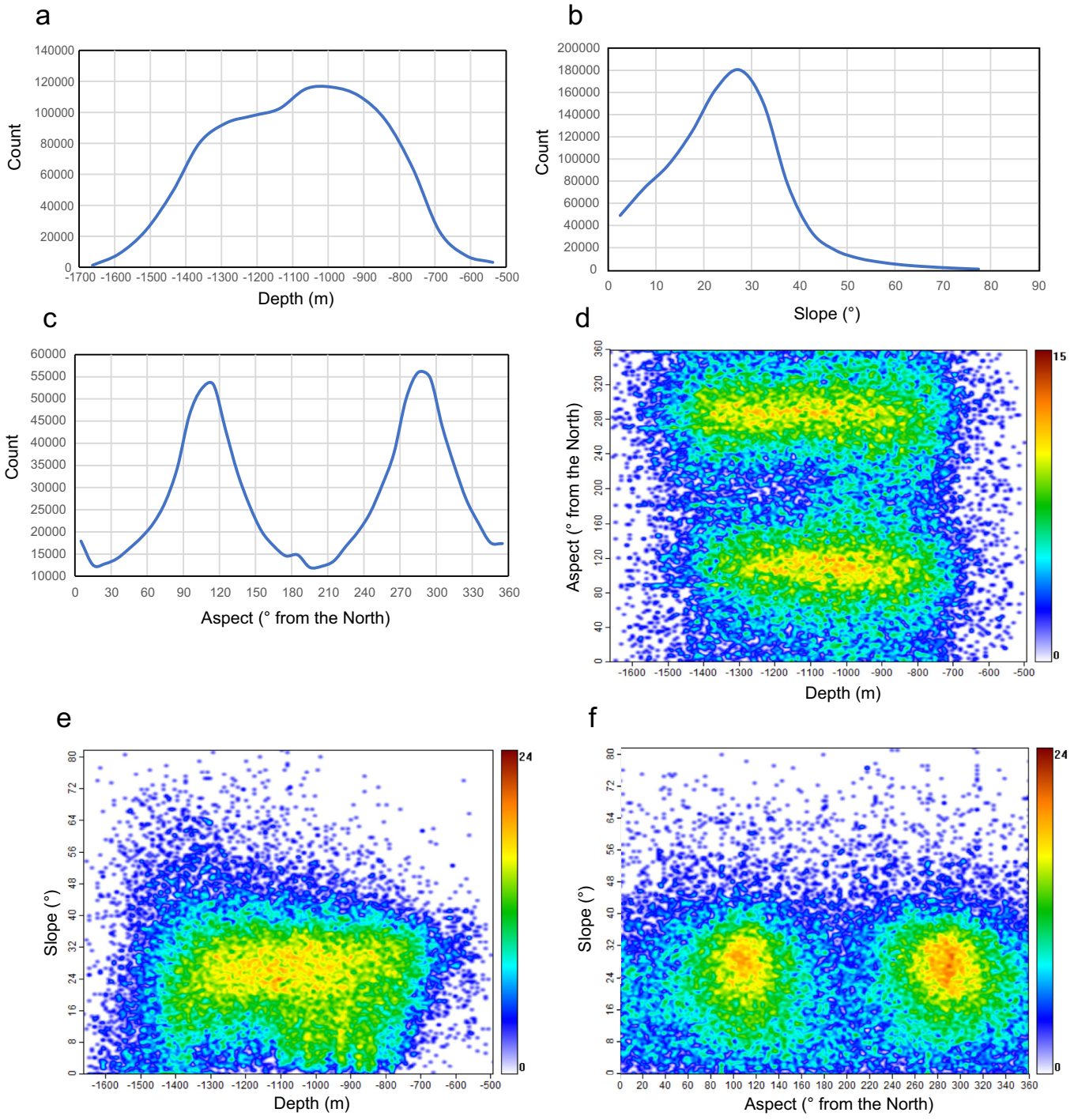

Fig. 3. Results of the morphometric analysis. (a) Depth vs number of 5 m × 5 m pixels of the DBM reported in Fig. 2 right. (b) Slope vs number of 5 m × 5 m pixels of the DBM reported in Fig. 2 right. (c) Aspect vs number of 5 m × 5 m pixels of the DBM reported in Fig. 2 right. (d) Depth vs aspect density plot. (e) Depth vs slope density plot. (f) Aspect vs slope density plot.

structed the 11 km long and −150 to 250 m high volcanic cones located in the flat summit area along the MS axis between −1000 and −900 mbsl (Fig. 9). The morphological preservation of each eruptive fissure in terms of erosion, and roundness of morphologies and sediment cover changes along the entire sector from the very well visible and linear volcanic cone chain at north (fissure FB5) toward the branched southern fissures FB1–FB2 (Fig. 9), which are slightly covered by marine deposits and partially dissected. Considering the superimpositions of the products related to each eruptive fissure, the FB1–FB2 fissures seem to be the most ancient of the Sector B being also covered by the fissures FB3 and FB4 (difference of elevation of about 70–90 m; Fig. 8b and 9). The fissure FB1 could be related to one of the most important eruptive episodes of the MS summit activity as it develops for a length of 5 km along a N10°E strike (Fig. 7b and 9). FB1 is characterized by some small cone-like morphologies possibly covered by marine deposits. As a further element, a larger, up to 150 m elevated volcanic cone dissected by a flank collapse of its eastern flank occupies the middle

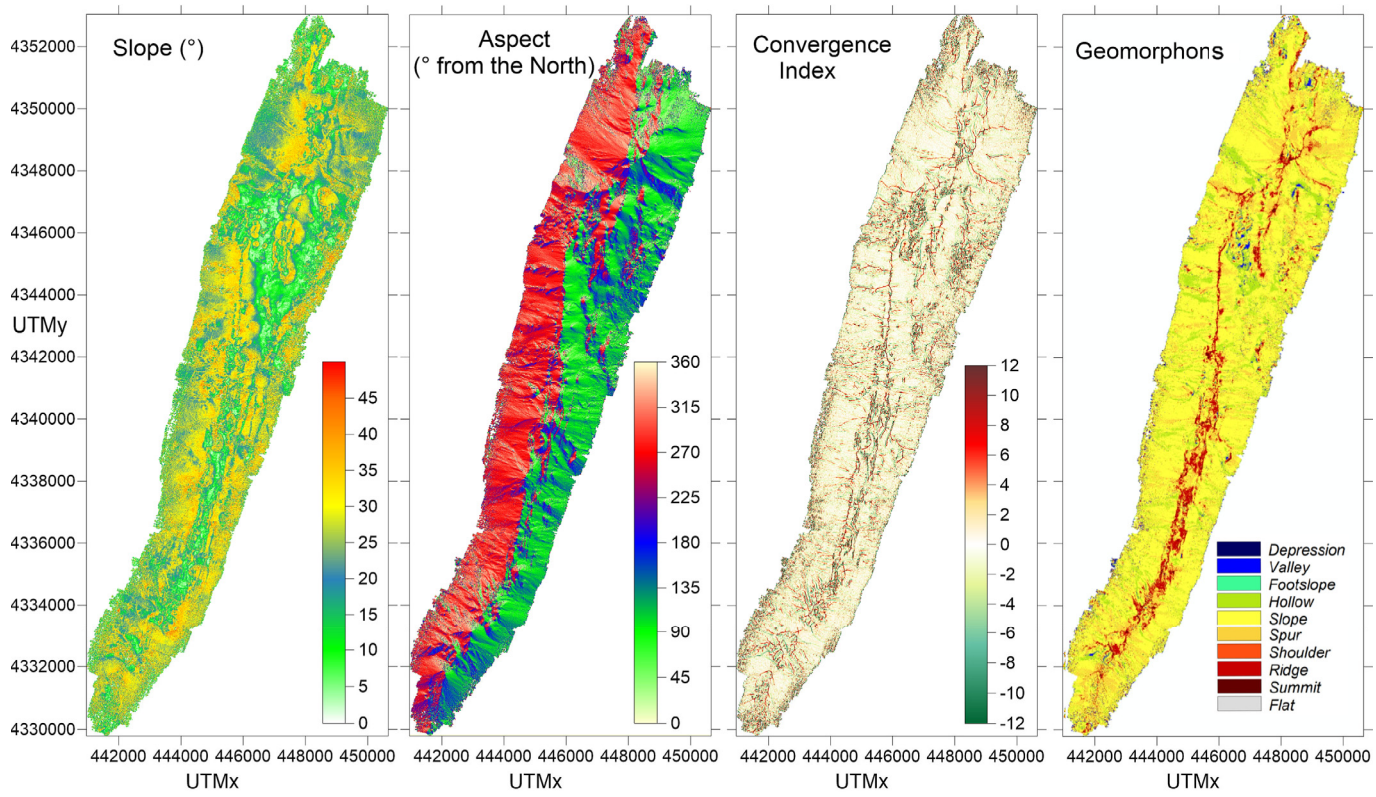

Fig. 4. Slope, Aspect, Convergence Index and Geomorphons maps of the MS DBM reported in Fig. 2 right.

position of this fissure. The small (1-km-long) and partially covered fissure FB2 shows a N20°E strike and it is covered by the fissure FB3, which has a 70 m higher summit and it is about 2 km long. The fissures FB4 and FB5 form a 5 km long positive morphology striking N5°E (Fig. 7b and 9). Some small cone-shaped morphologies on the mid flank of the edifice represent part of the covered products of the fissure FB4. The very fresh morphology of FB5 suggests that this fissure represents the more recent eruptive episode within sector B (Fig. 9). Summarizing all these observations, volcanic activity at MS migrated from south to north within sector B.

Sector C presents a more complex morphology mainly related to the intersection of four segmented eruptive fissures each one showing the same above described morphology of the volcanoes in Sector B. The length of the segmented fissures in Sector C ranges between 0.7 km and 1.5 km, and the strike varies from N1°E to N °38°E, with the two main parallel segments striking N30°E. No relationships exist between the eruptive fissures of the Sectors B and C. The fissure FC5 forms two very fresh ellipsoidal, up to 200 m high volcanic cones reaching –625 mbsl (Fig. 8c). The northernmost cone has two clearly visible craters on its top and the cone-like shape is well preserved. The southern cone is dissected by fractures and small flank collapses (Fig. 9). On the basis of the morphological and geometrical features, the fissure FC5 can be considered as the younger one among the fissures of the Sectors B–C. This suggests a northward migration of volcanic activity.

4.2.2. Polygenetic central volcanoes

Polygenetic volcanic edifices, as defined by Smith and Németh (2017), crop out in the sectors A and D (Fig. 9). They are characterized by large cones with flanks (average slopes 28°) up to –700 m high. Their flanks are partially dissected by collapses or caldera-like structures. Sector A presents two major central volcanoes, generally elongated along a N35°E direction. They show an elevation of ca. 450 m (CV1, from –1325 m to –875 mbsl; Fig. 9) and 250 m (CV2, from –965 m to –718 mbsl; Fig. 9) above their base, which is constituted by an ancient volcanic succession of MS deeply dissected by scars. Little of the pristine volcanic morphology is preserved, being the flanks covered by marine sediments. This is also testified by their summit portions, where the crater depressions are filled by sediments and not identifiable. Both the central volcanoes of Sector D present collapse-type structures on their southwestern flanks, whose origin, however, cannot be unequivocally attributed to a single mechanism.

The most important central volcano of the whole MS is CV3 in Sector D (Fig. 7b, 8d and 9). The elevation of this complex is of about 650–700 m ranging from –1150/–1200 m to –491 mbsl, starting from a base given by the ancient volcanic products of MS (>1 Myr). The DBM shows that this volcano is very heterogeneous as formed by (at least) three superimposed edifices, which are deeply dissected toward NW and whose semi-conical shape is still visible in their SE sectors (CV3a–c in Fig. 8d and 9). Notably, the shape of the collapses is very different from those of sector A, since they involve most of the edifice rather than a specific sector. Deposits possibly related to these collapses are lacking and the scarp of the collapses involves the summit portions of CV3 volcano. All these features lead us to propose that the scarps defining the CV3a–c collapses are related to caldera forming processes. As for subaerial caldera forming processes, these collapses could be associated with a vertical sinking of magma chamber(s) after/during an eruption or a cycle of eruptions of considerable volume. At MS, the arcuate scarps suggest 3 major events of caldera collapse. CV4 is a volcano nested within the composite caldera of CV3a.

Assuming that the relative age of activity is associated with the amount of (a) dismantling of the volcanic edifice and (b) the cover of marine sediments, as previously reported, the younger central-type edifice of MS is probably CV4.

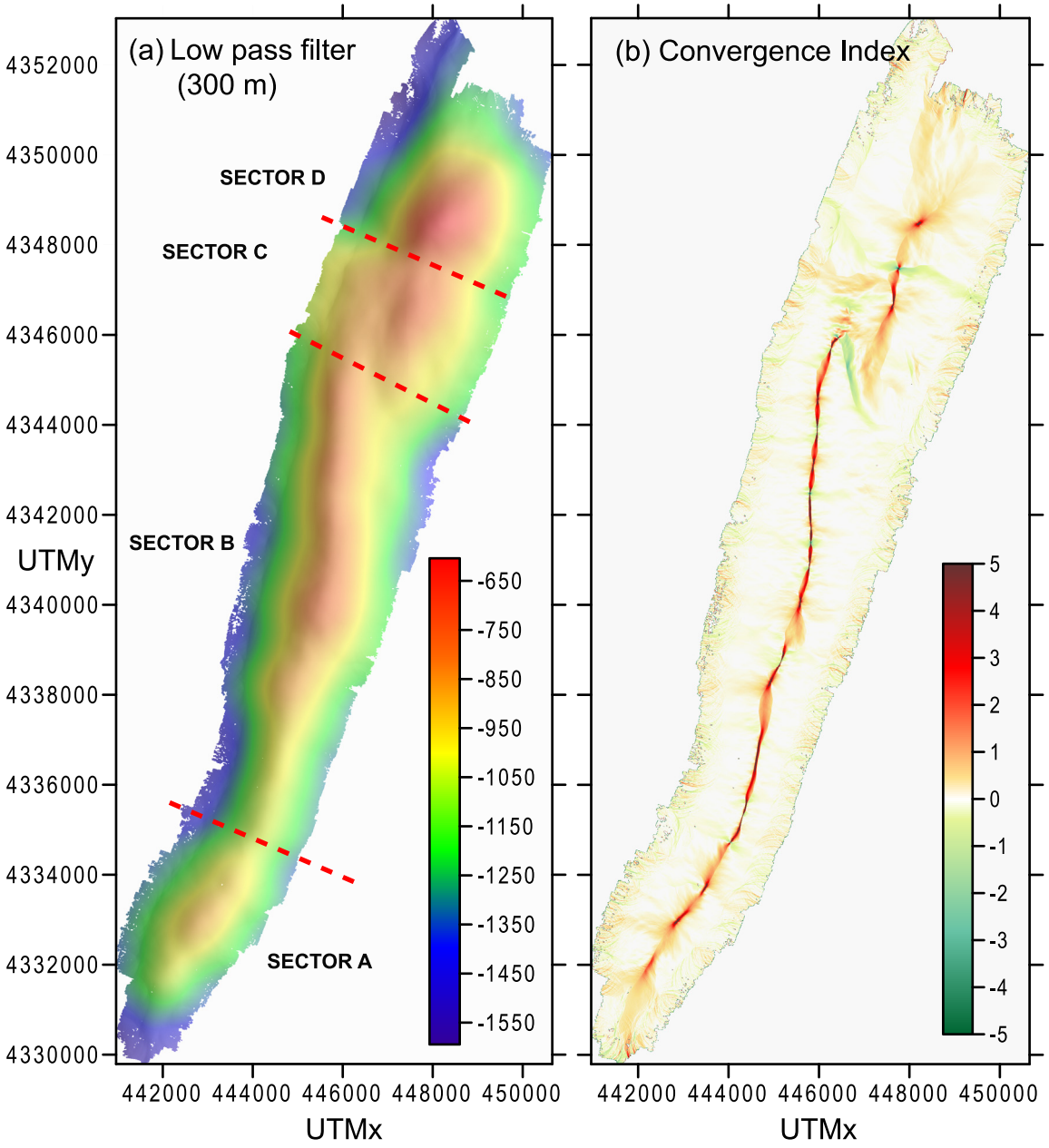

Fig. 5. (a) Low pass filtered (300 m) bathymetry of the MS DBM reported in Fig. 2 with identification of the morphological sectors A to D defined in the text. (b) Convergence index of the low pass filtered bathymetry sown on the left.

4.2.3. Lava flows, monogenetic cones and hydrothermal mounds

The MS volcanism also produced composite fields of monogenetic cones and lava flows, variably distributed among the considered sectors (Fig. 9). Up to 200–250 m high cones concentrate in sector C (Fig. 9), where they appear associated with short segments of eruptive fissures (e.g., FC4; Fig. 9). Lava flows outcrop in the sectors B, C, and D and cover about 4.23 km^2. Their morphology is quite well visible especially at the base of steep slopes, where the lava flow thickness increases. In the sectors B and C, lava flows are poured out from specific points of the eruptive fissure, whereas in sector D they are emitted from the summit of the central volcanoes.

Our newly presented DBM on MS also confirms the presence of a large hydrothermal field, occurring in the here-called sector C, and made up by more than 25 mounds, i.e. small and rounded hillocks (Fig. 9). The position of these mounds coincides with the position of fumarolic activity registered by Dekov and Savelli (2004), and with an area of negative magnetic anomaly detected by Cocchi et al. (2009) and Caratori Tontini et al. (2010) and attributed to hydrothermal demagnetization by Caratori Tontini et al. (2014) and Ligi et al. (2014) by modelling near-seafloor magnetic data.

4.2.4. Faults and landslide scars

Normal faults morphologically defined by sub-parallel NNE–SSW striking inward dipping scarps develop in the sectors A and B (Fig. 6). The faults are almost exclusively present on the ESE flanks of MS (Fig. 8b) with the vertical offset not exceeding 50 m,

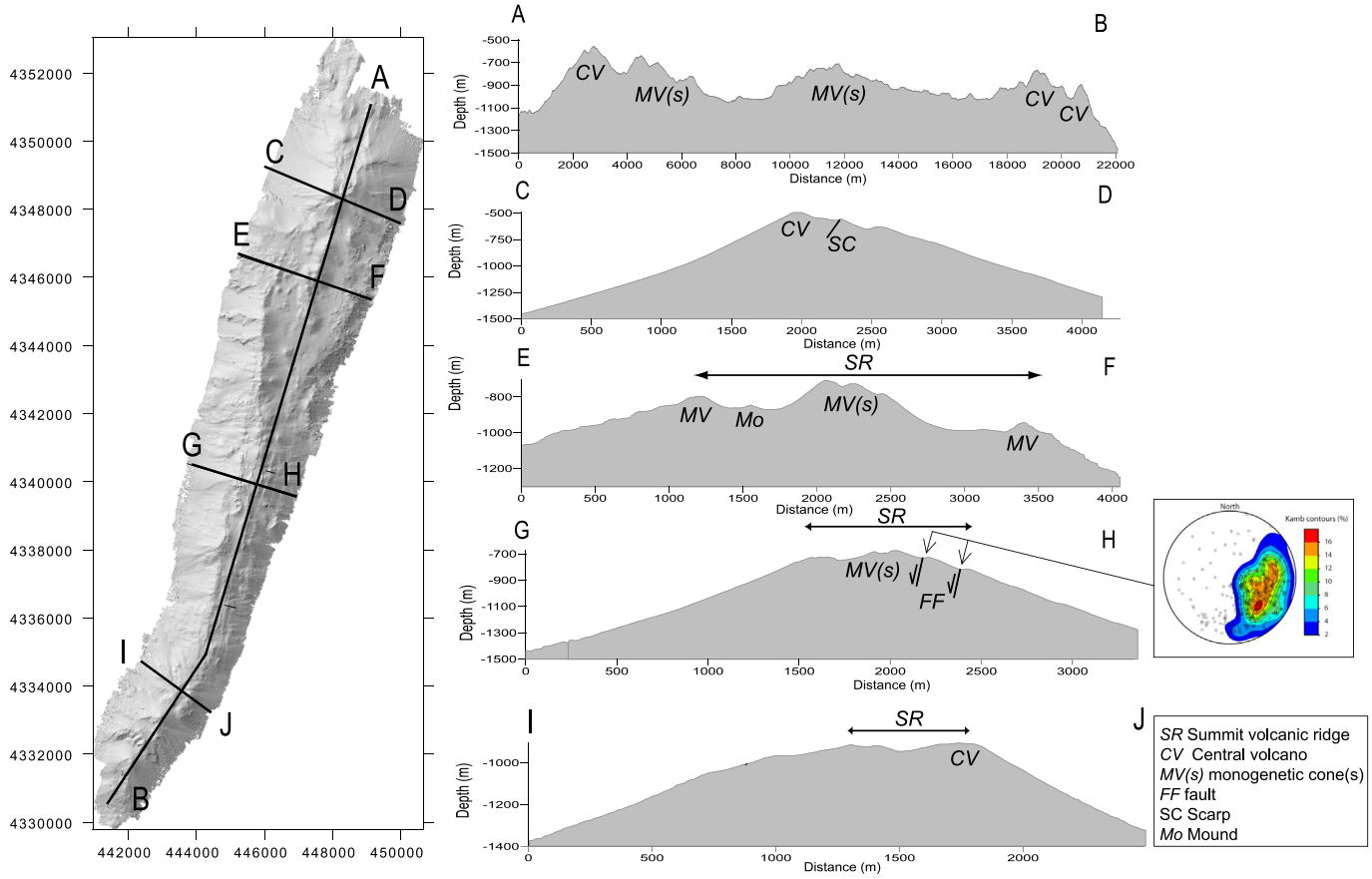

Fig. 6. Traces (left) and morphological profiles (right) crossing the 5 m × 5 m DBM of MS reported on the left. The density plot of the poles to the fault relative to the fault scarps reported on the profile G – H has been constructed from the aspect and slope values of the fault plane. The different volcanic and tectonic structures have been identified from the analysis of data reported in Figs. 2 and 4.

a value representing a minimum estimate because of the partial sedimentary cover of the MS flanks. Especially in Sector B, the occurrence of normal faults has led to the formation of a smooth flat area of the ridge on which the FB1–3 eruptive vents develop.

Morphological scars characterize the southernmost sector A (Figs. 5–9) which, following the above discussed relative age of the MS volcanic structures, is also the locus of the less recent volcanic activity. If the location and main strike of the MS volcanic, volcano-tectonic and tectonic structures are taken into account, the development of the scars are not associated with these structures. The scars are mainly controlled by the slope of the MS flanks. As a result, gravity instability processes of old volcanic slopes can be invoked for the sliding of the MS summit area.

5. Discussion

5.1. Evolution of volcanic landforms

One of the most important results of the above presented analysis is the relative chronological evolution of the volcanic activity at MS, which progressively shifted northward from the southernmost portions of the complex. This conclusion is also supported by the stratigraphic observations of Iezzi et al. (2020), which relate the cones of the central-northern MS sector to the more recent (2–3 ka; Iezzi et al., 2020) tephra emissions and with the still-occurring hydrothermal activity (Dekov and Savelli, 2004). This latter is also testified by the occurrence of mounds in sector C (Fig. 9).

Morphologies of sector A are the older volcanic structures of the summit portion of MS. They consist of volcanic edifices covered by sediments and affected by flank collapses, which also affected their summit areas, where evidence of the pristine craters and vents are not preserved.

The sector B of MS is related to prevalent fissural activity developing along a NNE–SSW preferred strike and forming well preserved ridges still not completely covered by marine sediments. Particularly, the degree of morphological preservation of the volcanic landforms of each eruptive fissure increases toward the north. One of the most important features of the southern tip of sector B sector is the presence of two different stacked branches (FB1–3 in Fig. 7), which, moving toward the North, coincide with FB4 which is partially superimposed by FB5 (Figs. 7 and 9). This means that the flat summit of Sector B has been affected by at least 2 subsequent major fissural events, now testified by the up to 5 km long eruptive ridges.

The migration of volcanic activity toward the northern portions of MS is also confirmed by the volcanic landforms of sector C (Fig. 8c). Here, although volcanic centers are disposed of along a NNE–SSW strike, they are not related to the injection of a km-scale dyke. Their (from one to two order smaller) lengths suggest the ascent of magma along pre-existing cracks of local significance. We propose that the parallel development of FC1-2–5 and of FC3-4 fissures is related to magma injection along the borders of a pre-existing ridge depression, which explains the flat morphology of the summit area of sector C with respect to that of the northern

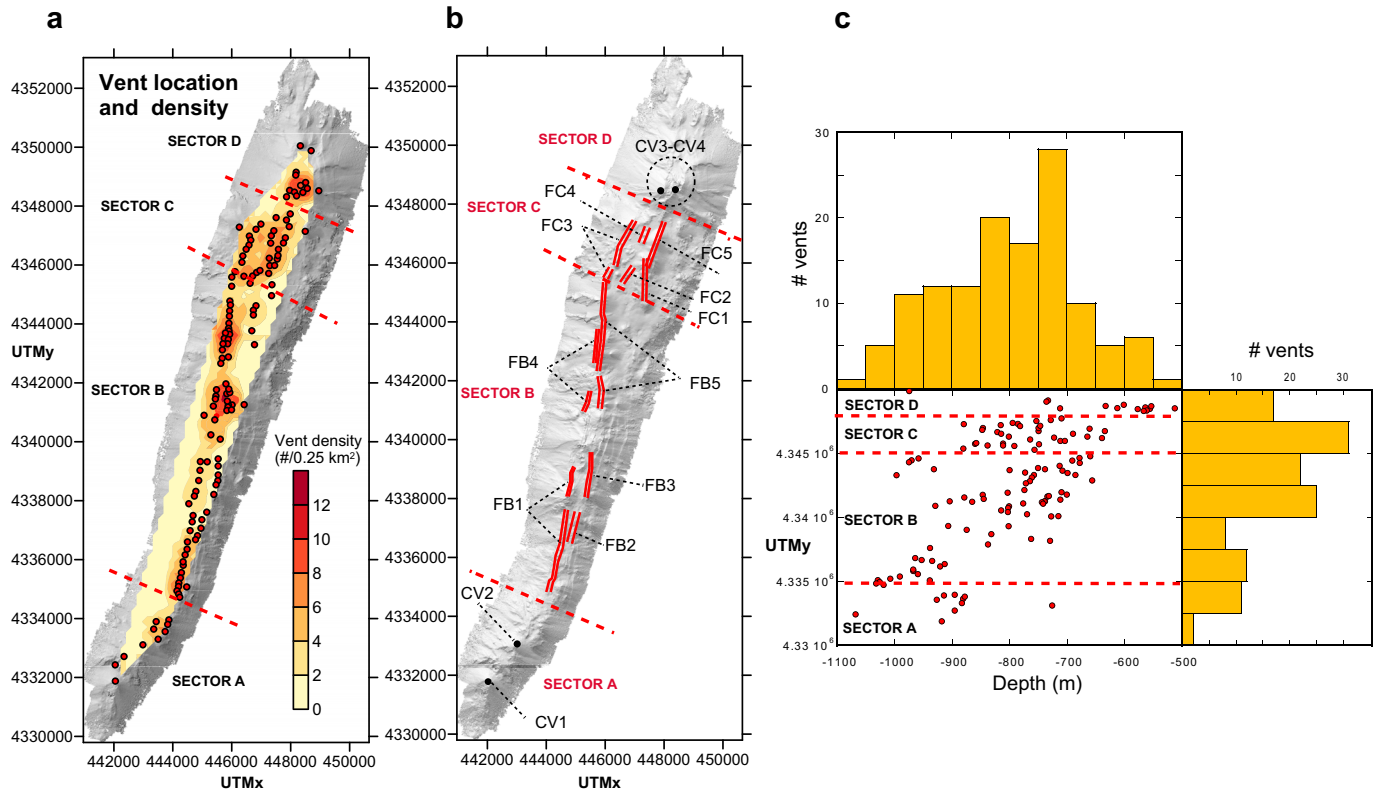

Fig. 7. (a) Map of the location of the volcanic vents and vent density obtained from the analysis of the 5 m × 5 m DBM of MS reported in Fig. 2. (b) Map of the MS eruptive fissures discussed in the text. (c) Distribution of the MS vents with latitude and depth. Note the different distributions in the sectors A to D.

and southern ones. Volcanic activity formed 200-m-high scoria cones with still preserved, sometimes breached craters from which lava flows were emitted (Fig. 9).

The morphological analysis of sector D has revealed the occurrence of scars indicative of major flank collapses of the main central volcano of MS (CV3 in Figs. 7 and 8). The overall morphology of the main central volcano is consistent with caldera-forming processes. The semi-circular morphology of the coalescing scars and their near-vertical slopes, along with the lack of block-like or hummocky-like deposits due to rock failure and the presence of a nested volcano within the scar, are all evidence of moderate caldera collapses. In subaerial environments, calderas are typically associated to the emptying of a shallow magma reservoir, and, in particular, to the partial collapse of its roof after an important eruptive event. If this result is joined to the observation that (a) morphological evidence of major collapse events is lacking in the sectors B and C, and (b) major flank collapses in sector A affect only ancient edifices, a new important factor of volcano hazard arises at MS. The trigger of a possible tsunamis due to caldera formation, which up to now has been only related to gravitational failures of the MS flanks (Gallotti et al., 2021) or to surficial seafloor sliding phenomena (Ventura et al., 2013), could also be now related to the onset of a caldera collapse after an eruptive event. In terms of hazard, our data add to these two scenarios the possible development of caldera collapses potentially able to produce tsunami events. Therefore, caldera collapses must be considered within the possible factors of instability of MS, especially in the case of a renewal of volcanic activity from the central volcanoes. Evidence of past gravity slides also characterizes the MS flanks, but the size of such slides suggests prevailing surficial seafloor sliding episodes.

5.2. The control of tectonics on volcanic landforms

The axial sector of MS consists of aligned cones, central volcanoes located at the northern and southern tip of the spreading ridge and an hydrothermal area occurring in the central-northern sector. The aligned cones represent the surface expression of deeper dikes, which, as result, form the shallower plumbing system of MS. When the whole here-presented morphological analysis is compared to a general scheme proposed by Tibaldi (2015) for the different types of plumbing system of volcanoes, we conclude that the MS axial portion mainly consists of a swarm of sub-parallel dikes. This is especially true for the central sector (Sector B in Figs. 4–9), where different, up to 5 km long fissures show the same strike (Fig. 8d). Such mechanisms of emplacement, and then the linear and symmetric growth of MS (Fig. 3c–d), is associated with a strict control by the tectonics, which, in the Marsili BAB, is governed by a ENE–WSW extension (Savelli, 2001; Ventura et al., 2003).

The progressive change of strike of the MS axial ridge from NNE–SSW to N–S for the southern sector in the central-northern sector C could be explained in two ways. In terms of fracture mechanics, changes of strikes at the tip of a crack do not develop if the tensile stress parallel to the crack T is 0, whereas a curvature of the crack strike is expected at $T > 0$ (Huajian and Cheng-Hsin, 1992). This may occur because of the anisotropy in the surrounding rocks, or variation of fracture resistance with respect to the crack orientation. At MS, the change in strike from NNE–SSW to N–S of the main ridge occurs in correspondence of the hydrothermal area and the onset of the northern, overlapping NNE–SSW striking ridges (Sector D). Therefore, a change in the fracture resistance due to hydrothermal fluids and $T > 0$ due to the occurrence of the hydrothermal system and the northern, right-sided, overlapping NNE–SSW ridge is expected. We can not *a priori* exclude that

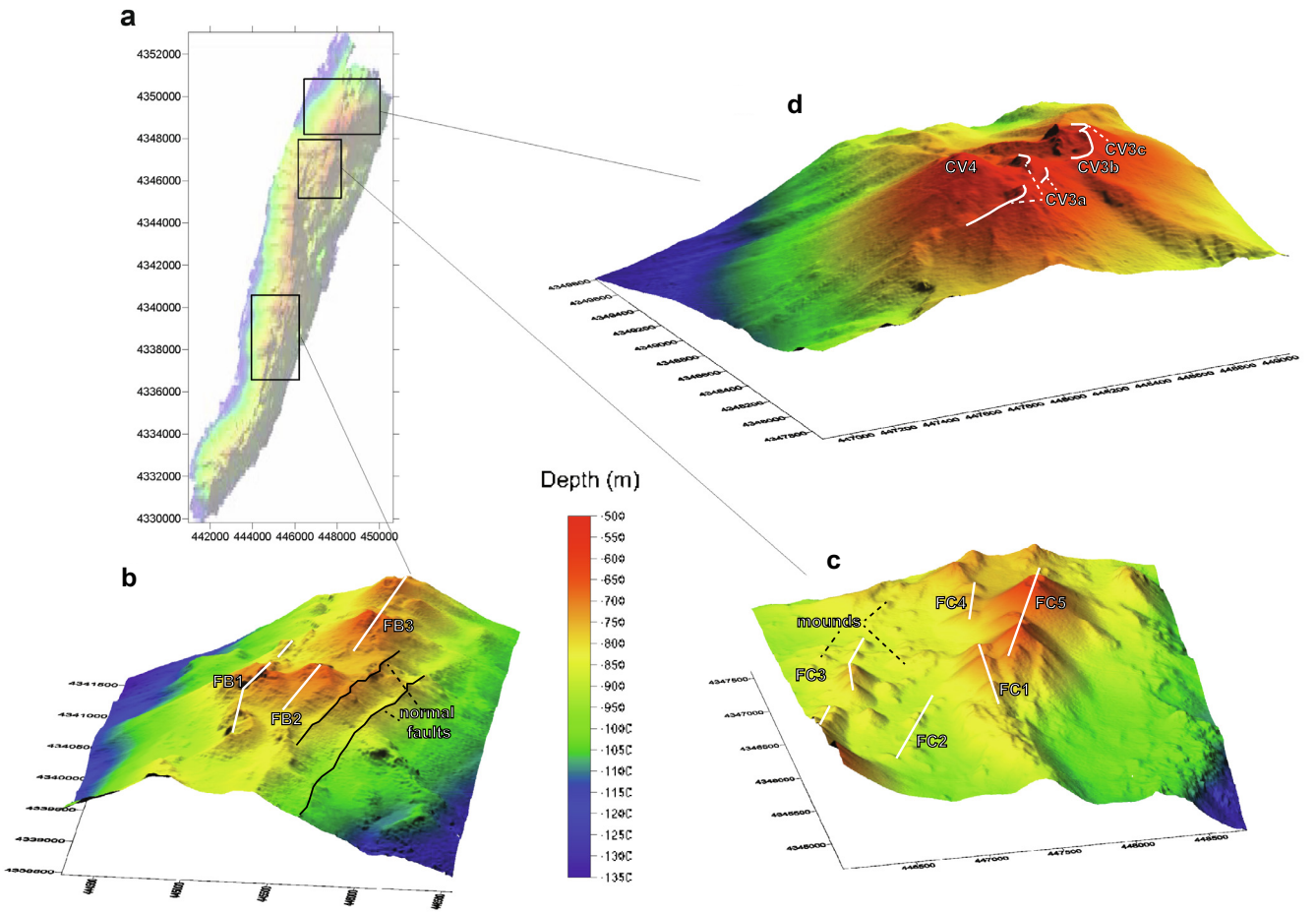

Fig. 8. (a) Location map of the 3D models of the MS DBM of Fig. 2 right. (b) Aligned cones and inward dipping faults in sector B. (c) Aligned cones and mounds in sector C. (d) Nested central volcano with a caldera-like structure defined by westward facing scarps in sector D. See text for a discussion.

the change in strike is associated with a deeper, crustal discontinuity located below MS. However, this latter hypothesis is not supported by the available geophysical data being the magnetic anomalies parallel to the general NNE–SSW strike of whole MS (Cocchi et al., 2009). In addition, in spreading ridges where transform faults do not exist (e.g., the Terceira and Reykjanes ridges), the control on segmentation is due to local tectonics instead of mantle or crustal discontinuities (van Wijk and Blackman, 2007). On the other hand, the occurrence of changes in strike (curvature) at the end of one or both overlapping spreading centers is a common feature of mid-ocean ridges (Tentler, 2003), where overlapping non-parallel segments tend to coalesce and one of their tips propagates toward the other fracture. This represents a first step in the structural evolution leading to the formation of transform faults (Gerya, 2012). At MS, the area of overlap between the two ridge segments is characterized by morphological (mounds), geophysical (negative magnetic anomaly, seismicity D'Alessandro et al., 2009) and direct observations (Dekov and Savelli, 2004) evidences of hydrothermal emissions. According to Pollard and Aydin (1984), the mean stress in the zone of overlapping ridges, i.e. dike zones, is tensile, and this allows the ascent of fluids and the formation of flat or depressed zones between the ridges. This mechanism could explain the occurrence of the flat area between the two overlapping spreading segments of the MS central-northern sector C. The eastern, NNE–SSW elongated ridge (FC1 and FC55 in Fig. 7b and 8b) of the sector C is constituted by aligned cones that are emplaced within a crack dissecting an older vent alignment. The northernmost of these new cones (FC5 in Fig. 7b) is responsible for the more recent tephra emissions at MS (2–3 ka; Iezzi et al., 2020). This indicates that the above defined ridge is still active and, as such, focuses the present-day spreading of MS. One interesting feature of MS is the occurrence of the central volcanoes at the northern and southern tips (Sectors A and D). Central volcanoes characterize the spreading zones and continental/oceanic rifts and may form by (i) coalescence of elongated ridges (Romer et al., 2021), (ii) rapid injections of dikes that alter the normal stress field allowing the formation of sills and magma chambers (Gudmundsson, 1990), or (iii) collapse of the flanks of the fissural feeding systems, that allows the shallow emplacement of magma and central volcanoes (Carracedo et al., 2011). However, these mechanisms cannot explain the occurrence of central volcanoes at the tip of the MS spreading ridge. The mechanisms (i) and (ii) are generally invoked for volcanoes located at the center of the ridges, and the mechanism (iii) is associated with large scale sector collapses of the fissural systems. At MS, evidence of flank collapse of the fissural feeding systems is lacking although geomorphological evidence of flank collapses characterize the central volcanoes. At a larger scale, the MS ridge may be considered as a big magma-filled crack at the tips of which the magma upraised with lower velocity with respect to its center. This implies higher magma residence times, rapid cooling at the dike tips, and, as a consequence, increase of magma viscosity (Wylie et al., 1999). In addition, Jones and Llewellin (2021) find that an increase of magma viscosity or a decrease in the dyke width at its tips pushes a fissural eruption

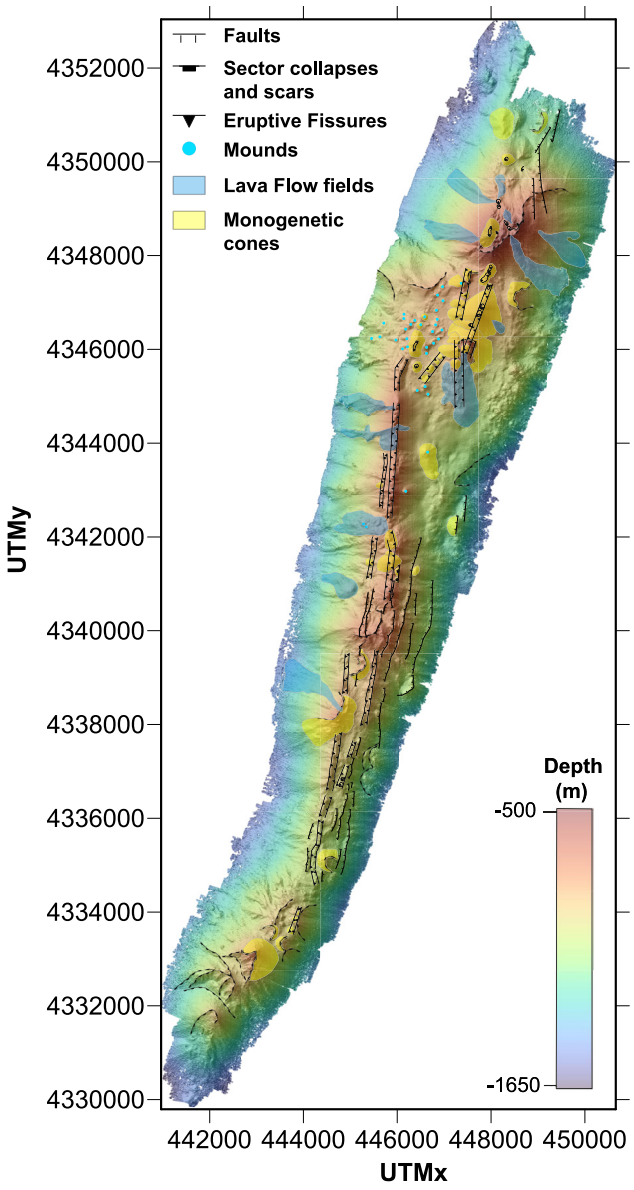

Fig. 9. Map with representation of all the morphological volcanic and geological elements of the studied area of Marsili seamount.

towards tipping points and vent localization. These interrelated mechanisms allow the formation of a magma storage zone and the focusing of magma in sub-circular conduits, which are prerequisites for the formation of central volcanoes. Taking into account these models, the emplacement of fissural dykes on of Sector B may represent the volcanic expression of the larger maximum tensile stresses within the area, the central big volcanoes of sector D those with the minimum ones, whereas the monogenetic cones of sector C would represent the response to relative intermediate stresses between adjacent sectors. These processes are also present in subaerial, mature continental rifts such as the northern sector of the Main Ethiopian Rift where a prolonged regional extension formed 4 volcano-tectonic segments characterized by fissural morphologies in their central portions and central volcanoes at their tips (Nicotra et al., 2021). In light of these considerations, we propose that MS central volcanoes form according to the above outlined mechanism(s).

As concerns the tectonic structures, only two major NNE–SSW striking and WSW dipping normal faults have been recognized in the eastern flank of MS. This feature could suggest that, at least in the past, MS was affected by an asymmetric spreading toward the east. This hypothesis is consistent with the general eastward opening of the Marsili back-arc basin (Doglioni, 1991; Faccenna et al., 1997; Cocchi et al., 2017). However, the length of these sub-parallel faults is of only 6–7 km over a surveyed length of the MS DMB of 22 km and the results of the morphometric analysis indicate a general symmetry in the MS flanks. We conclude that the above proposed hypothesis holds at a reduced spatial scale with only the central sector of MS partly affected by an asymmetric spreading phase.

5.3. The MS growth and its relation with the geodynamics

The MS accretion rate from 2.1 $\times$ 10^{-3} km^3/yr and 3.4 $\times$ 10^{-3} km^3/yr during the late Matuyama and Jaramillo Chrons to 4.21 $\times$ 10^{-3} km^3/yr during the Brunhes Chron is associated to a decrease in the spreading rate of the Marsili BAB from 3 cm/yr to about 1.8 cm/yr (Cocchi et al., 2009). This testifies the increasing relevance of the volcanic output with respect to the regional scale tectonic extension, thus explaining the poor evidence of tectonic

structures on MS. The general morphology of MS resembles that observed in fast spreading ridges, which are characterized by a well developed axial ridge without a summit valley (Macdonald, 1982; Püthe and Gerya, 2014). However, the above reported spreading rate values of the Marsili BAB are consistent with those reported for slow MOR spreading ridges (spreading rate between 1.5 and 5 cm/yr; Olive and Dublanchet, 2020) and consistent with spreading rates of other back-arc basin worldwide. These authors show that the ratio of magmatically accommodated extension to total plate separation *M* of slow spreading ridges may be comparable to those of fast spreading ridges, i.e., *M* = 0.9, which implies that slow spreading ridges may have a magmatic output large enough to produce inflated structures as MS. This interpretation is supported by the observed increase in MS magma output rate, associated with a decrease of the Marsili BAB spreading rate. Finally we remark that MS shows, on a spatial scale of a few tens of kilometers, the same complexity of larger scale back-arc spreading ridges as the Mariana back-arc in the West Pacific, which develops for a length of hundreds kilometers (Anderson et al., 2017). Such complexity includes dominantly magmatic segments, partly overlapping ridges, and embryonic development of transform faults, hydrothermal vents, fissural and central-type volcanoes. In addition, the morphology of the southern Mariana back-arc is consistent with those of fast-spreading mid-ocean ridges, despite its emplacement is characterized by a slow spreading rate. This contrast between the triggering spreading rates and the resulting morphology is also recognized at MS. In the case of the Mariana back-arc, these features are interpreted to reflect the additional input of arc magmas from the nearby volcanic front. This hypothesis also holds for MS, which is located just above the 400 km deep portion of the subducting Ionian slab below the Tyrrhenian Sea and at a distance of less than 100 km from the Aeolian volcanic arc (Fig. 1). The available geochemical data on MS show that the basaltic, andesitic, and trachytic magmas evolve from a heterogeneous mantle source in which calc-alkaline magmas with an Island Arc Basalts (IAB) signature mix with a Ocean Island Basalt (OIB) component (Trua et al., 2011). This latter represents the mantle source associated with the back-arc spreading. Therefore, the increase of the accretion rate of MS can be due to the addition of a subduction component to the mantle source.

6. Conclusions

The results of this study can be summarized in the following main points:

(1) The NNW-SSE elongated MS spreading ridge consists of four main sectors characterized by different morphologies. The southernmost and northernmost sectors are constituted by central-type volcanoes whereas the aligned cones of the central sectors represent swarms of sub-parallel dikes. The northernmost central volcano formed within a caldera-type depression. Therefore, possible volcano-tectonic collapses should be considered in the evaluation of tsunami-related hazards at MS.

(2) The MS central-northern sector includes overlapping spreading ridges and active hydrothermal manifestations. This is the youngest sector of MS because of its fresh morphology, historical volcanism and active fluid emissions. Faults parallel to the main MS ridge outcrop on the eastern flank of MS testifying a weak asymmetric (toward the east) spreading of the MS ridge, at least of its central portion.

(3) The observed change in strike of the MS axial ridge from NNE–SSW to N–S from south to north could be related to a change in the fracture resistance due to occurrence of hydrothermal fluids promoting a tensile stress parallel to pre-existing cracks. The overlapping, non-parallel ridge segments of the MS central-northern sector tend to coalesce. This arrangement may prelude the growth of a transform-type fault. The MS hydrothermal activity develops on a flat area located between the above defined two overlapping segments. These features well fit the results from numerical models of ridge interaction, where a tensile strain allows the ascent of fluids from depth and the development of flat/depressed morphologies.

(4) An increase of the magma output rate associated with a decrease of the back-arc spreading rate explains the high vertical/horizontal growth of MS. The occurrence of fissure volcanism along the MS spreading ridge and central-type volcanoes at the MS northern and southern tips is due to the rapid magma cooling at the tips of the ridge with consequent vent localization phenomena allowing the storage of magma at depth and the formation of sill-like magma storage zones and sub-circular conduits.

(5) MS shows spreading rates values compatible with those of the MOR slow spreading ridges, but its morphological features are more consistent with those of fast spreading ridges. These two features also characterize other, more extended back-arc spreading settings, like the Mariana in Western Pacific. In both Mariana and MS, despite the different spatial scale, the increase in the ridge accretion rate is related to the progressive addition of a subduction-related component to a pure spreading, mantle source.

Further investigation on the volcanic and tectonic landforms of other BAB spreading ridges should be carried out to better understand the mechanisms of formation of such relevant structures, whose complexity testifies the concomitant action of different tectonic, magmatic, and gravity processes. In addition, the integration of morphological and, when available, geochemical and geophysical data could give us information on how deep seated processes influence the submarine landforms of BAB.

CRediT authorship contribution statement

Eugenio Nicotra: Conceptualization, Formal analysis, Investigation, Writing – Original Draft, Visualization. **Salvatore Passaro**: Methodology, Validation, Investigation, Resources, Writing – Review & Editing. **Guido Ventura**: Conceptualization, Methodology, Validation, Formal analysis, Investigation, Writing – Original Draft, Visualization, Supervision.

Declaration of Competing Interest

The authors declare that they have no known competing financial interests or personal relationships that could have appeared to influence the work reported in this paper.

Acknowledgments

This work has been funded by the Marine Hazard CNR Project. We thank the crew of “Urania” M/V for the continuous support and help. We really appreciated the editorial assistance of Dr. Inna

Safonova and the comments of the reviewer Dr. Fabio Caratori Tontini.

References

Aliani, S., Bortoluzzi, G., Caramanna, G., Raffa, F., 2010. Seawater dynamics and environmental settings after November 2002 gas eruption off Bottaro (Panarea, Aeolian Islands, Mediterranean Sea). Cont. Shelf Res. 30 (12), 1338–1348.

Anderson, M.O., Chadwick, W.W., Hannington, M.D., Merle, S.G., Resing, J.A., Baker, E.T., Butterfield, D.A., Walker, S.L., Augustin, N., 2017. Geological interpretation of volcanism and segmentation of the Mariana back-arc spreading center between 12.78°N and 18.38°N. Geochem. Geophys. Geosyst. 18, 2240–2274. https://doi.org/10.1002/2017GC006813.

Artemieva, I.M., 2023. Back-arc basins: A global view from geophysical synthesis and analysis. Earth Sci. Rev. 236, 104242. https://doi.org/10.1016/j.earscirev.2022.104242.

Beccaluva, L., Rossi, P.L., Serri, G., 1982. Neogene to Recent volcanism of the Southern Tyrrhenian-Sicilian area: implications for the geodynamic evolution of the Calabrian Arc. Earth Evolution Sciences 2 (3), 222–238.

Caratori Tontini, F., Cocchi, L., Muccini, F., Carmisciano, C., Marani, M., Bonatti, E., Ligi, M., Boschi, E., 2010. Potential-field modeling of collapse-prone submarine volcanoes in the southern Tyrrhenian Sea (Italy). Geophys. Res. Lett. 37 (3), L03305. https://doi.org/10.1029/2009GL041757.

Caratori Tontini, F., Bortoluzzi, G., Carmisciano, C., Cocchi, L., de Ronde, C.E.J., Ligi, M., Muccini, F., 2014. Near-bottom magnetic signatures of submarine hydrothermal systems at Marsili and Palinuro Volcanoes, Southern Tyrrhenian Sea, Italy. Econ. Geol. 109, 2119–2128. https://doi.org/10.2113/econgeo.109.8.2119.

Caratori Tontini, F., Bassett, D., de Ronde, C.E.J., Timm, C., Wysoczanski,, 2019. Early evolution of a young back-arc basin in the Havre Trough. Nat. Geosci. 12, 856–862. https://doi.org/10.1038/s41561-019-0439-y.

Carminati, E., Lustrino, M., Doglioni, C., 2012. Geodynamic evolution of the central and western Mediterranean: tectonics vs. igneous petrology constraints. Tectonophysics 579, 173–192.

Carracedo, J.C., Guillou, H., Nomade, S., Rodriguez-Badiola, E., Perez-Torrado, F.J., Rodriguez-Gonzalez, A., Paris, R., Troll, V.R., Wiesmaier, S., Delcamp, A., Fernandez-Turiel, J.L., 2011. Evolution of ocean-island rifts: The northeast rift zone of Tenerife, Canary Islands. Geol. Soc. Am. Bull. 123 (3–4), 562–584. https://doi.org/10.1130/B30119.1.

Claps, P., Fiorentino, M., Oliveto, G., 1996. Informational entropy of fractal river networks. J. Hydrol. 187, 145–156.

Cocchi, L., Caratori Tontini, F., Muccini, F., Marani, M.P., Bortoluzzi, G., Carmisciano, C., 2009. Chronology of the transition from a spreading ridge to an accretional seamount in the Marsili backarc basin (Tyrrhenian Sea). Terra Nova 21 (5), 369–374. https://doi.org/10.1111/j.1365-3121.2009.00891.x.

Cocchi, L., Passaro, S., Caratori Tontini, F., Ventura, G., 2017. Volcanism in slab tear faults is larger than in island-arcs and back-arcs. Nat. Comm. 8, 1451. https://doi.org/10.1038/s41467-017-01626-w.

Conrad, O., Bechtel, B., Bock, M., Dietrich, H., Fischer, E., Gerlitz, L., Wehberg, J., Wichmann, V., Bohner, J., 2015. System for Automated Geoscientific Analyses (SAGA) v. 2.1.4. Geosci. Model Development 8, 1991–2007. https://doi.org/10.5194/gmd-8-1991-2015.

Cressie, N.A.C., 1990. The Origins of Kriging. Math. Geol. 22, 239–252.

D'Alessandro, A., D'Anna, G., Luzio, D., Mangano, G., 2009. The INGV's new OBS/H: Analysis of the signals recorded at the Marsili submarine volcano. J. Volcanol. Geoth. Res. 183 (1–2), 17–29. https://doi.org/10.1016/j.jvolgeores.2009.02.008.

De Astis, G., Ventura, G., Vilardo, G., 2003. Geodynamic significance of the Aeolian volcanism (Southern Tyrrhenian Sea, Italy) in light of structural, seismological and geochemical data (Open Access). Tectonics 22 (4), 1040. https://doi.org/10.1029/2003tc001506.

Dekov, V., Savelli, C., 2004. Hydrothermal activity in the SE Tyrrhenian Sea: An overview of 30 years of research. Mar. Geol. 204, 161–185. https://doi.org/10.1016/S0025-3227(03)00355-4.

Doglioni, C., 1991. A proposal for the kinematic modeling of W-dipping subductions: possible applications to the Tyrrhenian-Apennines system. Terra Nova 3, 423–434.

Doglioni, C., Gueguen, E., Sabat, F., Fernandez, M., 1997. The western Mediterranean extensional basins and the Alpine orogen. Terra Nova 9, 109–112.

Drymoni, K., Russo, E., Tibaldi, A., Corti, N., Bonali, F.L., 2023. Dyke-induced graben formation in a heterogeneous succession on Mt. Etna: Insights from field observations and FEM numerical models. J. Volcanol. Geoth. Res. 433, 107712. https://doi.org/10.1016/j.jvolgeores.2022.107712.

Esposito, V., Andaloro, F., Canese, S., Bortoluzzi, G., Bo, M., Di Bella, M., Italiano, F., Sabatino, G., Battaglia, P., Consoli, P., Giordano, P., Spagnoli, F., La Cono, V., Yakimov, M.M., Scotti, G., Romeo, T., 2018. Exceptional discovery of a shallow-water hydrothermal site in the SW area of Basiluzzo islet (Aeolian archipelago, South Tyrrhenian Sea): An environment to preserve. PLoS One 13 (1), e0190710.

Faccenna, C., Mattei, M., Funiciello, D., Jolivet, L., 1997. Styles of back-arc extension in the Central Mediterranean. Terra Nova 9, 126–130. https://doi.org/10.1046/j.1365-3121.1997.d01-12.x.

Gallotti, G., Zaniboni, F., Pagnoni, G., Tinti, S., 2021. Tsunamis from prospected mass failure on the Marsili submarine volcano flanks and hints for tsunami hazard evaluation. Bull. Volcanol. 83, 2. https://doi.org/10.1007/s00445-020-01425-0.

Gerya, T., 2012. Origin and models of oceanic transform faults. Tectonophysics 522–523, 34–54.

Gudmundsson, A., 1990. Emplacement of dikes, sills and crustal magma chambers at divergent plate boundaries. Tectonophysics 176, 257–275.

Holt, A.F., Royden, L.H., 2020. Subduction dynamics and mantle pressure: 2. Towards a global understanding of slab dip and upper mantle circulation. Geochem. Geophys. Geosyst. 20, 08771. https://doi.org/10.1029/2019GC008771.

Huajian, G., Cheng-Hsin, C., 1992. Slightly curved or kinked cracks in anisotropic elastic solids. Int. J. Solids Struct. 29, 947–972. https://doi.org/10.1016/0020-7683(92)90068-5.

Iezzi, G., Caso, C., Ventura, G., Vallefuoco, M., Cavallo, A., Behrens, H., Mollo, S., Paltrinieri, D., Signanini, P., Vetere, F., 2013. First documented deep submarine explosive eruptions at the Marsili Seamount (Tyrrhenian Sea, Italy): a case of historical volcanism in the Mediterranean Sea. Gondw. Res. 25, 764–774.

Iezzi, G., Lanzafame, G., Mancini, L., Behrens, H., Tamburrino, S., Vallefuoco, M., Passaro, S., Signanini, P., Ventura, G., 2020. Deep sea explosive eruptions may be not so different from subaerial eruptions. Sci. Rep. 10 (1), 6709. https://doi.org/10.1038/s41598-020-63737-7.

Jasiewicz, J., Stepinski, T.F., 2013. Geomorphons–a pattern recognition approach to classification and mapping of landforms. Geomorphology 182, 147–156. https://doi.org/10.1016/j.geomorph.2012.11.005.

Jones, T.J., Llewellin, E.W., 2021. Convective tipping point initiates localization of basaltic fissure eruptions. Earth Planet. Sci. Lett. 553, 116637. https://doi.org/10.1016/j.epsl.2020.116637.

Karig, D.E., 1971. Origin and development of marginal basins in the western Pacific. J. Geophys. Res. 76 (11), 2542–2561. https://doi.org/10.1029/JB076i011p02542.

Kastens, K., Mascle, J., 1990. The geological evolution of the Tyrrhenian Sea: an introduction to the scientific results of ODP Leg 107. Proceedings of Ocean Drilling Program Science Results 107, 3–26.

Kelley, D.S., Baross, J.A., Delaney, J.R., 2002. Volcanoes, fluids, and life at mid-ocean ridge spreading centers. Annu. Rev. Earth Planet. Sci. 30, 385–491.

Li, S.Z., Suo, Y.H., Li, X.Y., Liu, B., Dai, L., Wang, G., Zhou, J., Li, Y., Liu, Y., Cao, X., Somerville, I., Mu, D., Zhao, S., Liu, J., Meng, F., Zehn, L., Zhao, L., Zhu, J., Yu, S., Liu, Y., Zhang, G., 2018. Microplate Tectonics: new insights from microblocks in the global oceans, continental margins and deep mantle. Earth Sci. Rev. 185, 1029–1064.

Ligi, M., Cocchi, L., Bortoluzzi, G., D'Oriano, F., Muccini, F., Caratori Tontini, F., de Ronde, C.E.J., Carmisciano, C., 2014. Mapping of seafloor hydrothermally altered rocks using geophysical methods: Marsili and Palinuro Seamounts, Southern Tyrrhenian Sea. Econ. Geol. 109, 2102–2117. https://doi.org/10.2113/econgeo.109.8.2103.

Lupton, J., De Ronde, C., Sprovieri, M., Baker, E.T., Bruno, P.P., Italiano, F., Walker, S., Faure, K., Leybourne, M., Britten, K., Greene, R., 2011. Active hydrothermal discharge on the submarine Aeolian Arc. J. Geophys. Res.: Solid Earth 116 (2), B02102. https://doi.org/10.1029/2010JB007738.

Lustrino, M., Duggen, S., Rosenberg, C.L., 2011. The Central-Western Mediterranean: Anomalous igneous activity in an anomalous collisional tectonic setting. Earth Sci. Rev. 104 (1–3), 1–40.

Macdonald, K.C., 1982. Mid-Ocean Ridges: fine scale tectonic, volcanic and hydrothermal processes within the plate boundary zone. Annu. Rev. Earth Planet. Sci. 10, 155.

Magrini, F., Diaferia, G., El-Sharkawy, A., Cammarano, F., van der Meijde, M., Meier, T., Boschi, L., 2022. Surface wave tomography of the central-western Mediterranean: New insights into the Liguro-Provençal and Tyrrhenian basins. J. Geophys. Res.: Solid Earth 127. https://doi.org/10.1029/2021JB023267.

Maher, S.M., Gee, J.S., Cheadle, M.J., John, B.E., 2021. Three-dimensional magnetic stripes require slow cooling in fast-spread lower ocean crust. Nature 597, 511–515.

Marani, M.P., Trua, T., 2002. Thermal constriction and slab tearing at the origin of a superinflated spreading ridge: Marsili volcano (Tyrrhenian Sea). J. Geophys. Res.: Solid Earth 107, 00285. https://doi.org/10.1029/2001JB000285.

Marani, M.P., Gamberi, F., Bonatti, E., 2004. From seafloor to deep mantle: architecture of the Tyrrhenian backarc basin. Memorie Descrittive Carta Geologica d'Italia, LXIV.

Nicotra, E., Viccaro, M., De Rosa, R., Sapienza, M., 2014. Volcanological evolution of the Rivi-Capo volcanic complex at Salina, Aeolian Islands: magma storage processes and ascent dynamics. Bull. Volcanol. 76, 840–864.

Nicotra, E., Viccaro, M., Donato, P., Acocella, V., De Rosa, R., 2021. Catching the Main Ethiopian Rift evolving towards plate divergence. Sci. Rep. 11, 21821.

Olive, J.A., Dublanchet, P., 2020. Controls on the magmatic fraction of extension at mid-ocean ridges. Earth Planet. Sci. Lett. 549, 116541. https://doi.org/10.1016/j.epsl.2020.116541.

Panza, G.F., Raykova, R.B., Carminati, E., Doglioni, C., 2007. Upper mantle flow in the western Mediterranean. Earth Planet. Sci. Lett. 257, 200–214.

Passaro, S., Milano, G., Disanto, C., Ruggieri, S., Tonielli, R., Bruno, P., Sprovieri, M., Marsella, E., 2010. DTM-Based morphometry of the Palinuro seamount (Italy, Eastern Tyrrhenian Sea): geomorphological and volcanological implication. Geomorphology 115 (1–2), 129–140. https://doi.org/10.1016/j.geomorph.2009.09.041.

Pollard, D.D., Aydin, A., 1984. Propagation and linkage of oceanic ridge segments. J. Geophys. Res. 89, 10017–10028. https://doi.org/10.1029/JB089iB12p10017.

Püthe, C., Gerya, T., 2014. Dependence of mid-ocean ridge morphology on spreading rate in numerical 3-D models. Gondw. Res. 25, 270–283.

Romer, R.H.W., Beier, C., Haase, K.M., Eberts, A., Hübscher, C., 2021. The evolution of central volcanoes in ultraslow rift systems: Constraints from D. João de Castro

seamount, Azores. Tectonics 40 (7), e2020TC006663. https://doi.org/10.1029/2020TC006663.
Rosenbaum, G., Lister, G.S., 2004. Neogene and Quaternary rollback evolution of the Tyrrhenian Sea, the Apennines and the Sicilian Maghrebides. Tectonics 23, TC1013. https://doi.org/10.1029/2003TC001518.
Sartori, R., 2003. The Tyrrhenian back-arc basin and subduction of the Ionian lithosphere. Episodes 26, 217–223.
Savelli, C., 2001. Two-stage progression of volcanism (8–0 Ma) in the Central Mediterranean (Southern Italy). J. Geodyn. 31 (4), 393–410.
Schliffke, N., van Hunen, J., Allen, M.B., Magni, V., Gueydan, F., 2022. Episodic back-arc spreading centre jumps controlled by transform fault to overriding plate strength ratio. Nat. Comm. 13, 582. https://doi.org/10.1038/s41467-022-28228-5.
Sdrolias, M., Muller, R.D., 2006. Controls on back-arc basin formation. Geochem. Geophys. Geosyst. 7, Q04016. https://doi.org/10.1029/2005GC001090.
Smith, I.E.M., Németh, K., 2017. Source to surface model of monogenetic volcanism: A critical review. Geochem. Soc. Spec. Publ. 446 (1), 1–28.
Solomon, S.C., Toomey, D.R., 1992. The structure of Mid-Ocean ridges. Annu. Rev. Earth Planet. Sci. 20, 329–366.
Stern, R.J., 2002. Subduction Zones. Rev. Geophys. 40 (4), 1012. https://doi.org/10.1029/2001RG000108.
Tamburrino, S., Vallefuoco, M., Ventura, G., Insinga, D.D., Sprovieri, M., Tiepolo, M., Passaro, S., 2015. The proximal marine records of the Marsili Seamount in the last 7 ka (Southern Tyrrhenian Sea back-arc, Italy) put constraints on the evolution of plumbing systems in declining back-arc spreading ridges. Global Planet. Change 133, 2–16.
Tan, Y.J., Tolstoy, M., Waldhauser, F., Wilcock, W.S., 2016. Dynamics of a seafloor-spreading episode at the East Pacific Rise. Nature 540 (7632), 261–265.
Tentler, T., 2003. Analogue modeling of overlapping spreading centers: Insight into their propagation and coalescence. Tectonophysics 376, 99–115.
Tibaldi, A., 2015. Structure of volcano plumbing systems: A review of multi-parametric effects. J. Volcanol. Geoth. Res. 298, 85–135.
Trua, T., Marani, P.M., Gamberi, F., 2011. Magmatic evidence for African mantle propagation into the southern Tyrrhenian back-arc region. In: Beccaluva, L., Bianchini, G., Wilson, M. (Eds), Volcanism and Evolution of the African Lithosphere. Spec. Pap. Geol. Soc. Am. 478, 307–331.
van Wijk, J.W., Blackman, D.K., 2007. Development of en echelon magmatic segments along oblique spreading ridges. Geology 35, 599–602. https://doi.org/10.1130/G23294A.1.
Ventura, G., Milano, G., Passaro, S., Sprovieri, M., 2013. The Marsili ridge (Southern Tyrrhenian Sea, Italy): An island-arc volcanic complex emplaced on a 'relict' back-arc basin. Earth Sci. Rev. 116 (1), 85–94. https://doi.org/10.1016/j.earscirev.2012.11.005.
Wei, S.S., Wiens, D.A., 2020. High bulk and shear attenuation due to partial melt in the Tonga-Lau back-arc mantle. J. Geophys. Res.: Solid Earth 125 (1), e2019JB017527.
Wylie, J.J., Helfrich, K.R., Dade, B., Lister, J.R., Salzig, J.F., 1999. Flow localisation in fissure eruptions. Bull. Volcanol. 60 (6), 432–440. https://doi.org/10.1007/s004450050243.